Magnetic Resonance in Medicine 57:1119–1130 (2007)

Longitudinal Gradient Coil Optimization in the Presence of Transient Eddy Currents

A. Trakic, F. Liu, H. Sanchez Lopez, H. Wang, and S. Crozier*

The switching of magnetic field gradient coils in magnetic resonance imaging (MRI) inevitably induces transient eddy currents in conducting system components, such as the cryostat vessel. These secondary currents degrade the spatial and temporal performance of the gradient coils, and compensation methods are commonly employed to correct for these distortions. This theoretical study shows that by incorporating the eddy currents into the coil optimization process, it is possible to modify a gradient coil design so that the fields created by the coil and the eddy currents combine together to generate a spatially homogeneous gradient that follows the input pulse. Shielded and unshielded longitudinal gradient coils are used to exemplify this novel approach. To assist in the evaluation of transient eddy currents induced within a realistic cryostat vessel, a low-frequency finite-difference time-domain (FDTD) method using the total-field scattered-field (TFSF) scheme was performed. The simulations demonstrate the effectiveness of the proposed method for optimizing longitudinal gradient fields while taking into account the spatial and temporal behavior of the eddy currents. Magn Reson Med 57:1119–1130, 2007.

Key words: eddy currents; MRI; gradient; FDTD; cryostat

During the pulsing of magnetic field gradients in MRI, multiexponentially decaying eddy currents are always induced within the conducting materials of the MR imager. Eddy currents in cold, highly conductive radiation shields of the superconducting magnet produce particularly long-acting effects relative to the image acquisition period (1–2). These secondary magnetic fields are known to cause spatial and temporal degradation of the gradient uniformity within the imaging volume, which often results in undesired misregistration and intensity-phase variations in both images and spectra.

With the recent push of MRI towards high signal-to-noise ratios (SNRs) and improved image resolution, tremendous efforts have been made to prevent and minimize the eddy-current fields. For instance, active screening is often engaged to minimize leakage fields and hence spatially and temporally complex residual eddy currents induced in the cryostat vessel (3–8). Unfortunately, the use of active shielding layer(s) occupies vital space inside the bore of the magnet, increases system cost, and reduces gradient efficiency. Furthermore, residual eddy currents are never completely removed through active shielding, and experimental compensation methods are also required for optimal results (9,10).

During the design of conventional gradient coils (cylindrical, planar, etc.), the current distributions in one or more gradient layers are commonly optimized to obtain a target gradient uniformity in the imaging volume while satisfying other design constraints such as minimum inductance, resistance, leakage fields, force, torque, and maximum gradient efficiency (1). Traditionally, these design approaches do not take eddy currents into direct consideration when optimizing the gradient coil. Consequently, during the pulsing of the gradient current, eddy currents are induced in the cryostat vessel and other conducting materials that lead to degradation of the target field uniformity and the field stability.

In 1986, Turner and Bowley (13) were among the first to introduce an analytical technique for passive magnetic screening. Their study considered spatial eddy-current variations in a thick, highly conductive, infinitely long aluminum shield as the secondary source contributing to target gradient fields. By varying the single-layer gradient coil positions to accommodate for the spatial presence of eddy currents in the metal sheet, they were able to show that good gradient uniformities can be obtained. However, the authors assumed that the skin depth in the aluminum shield was much smaller than the radial thickness of the screen, which resulted in a purely spatial problem description. Obviously, in a realistic cryostat vessel that often consists of more than one metal shield, the aforementioned assumptions are not always valid. Therefore, we believe that it is necessary to compute the exact spatial (radial, axial, and azimuthal) and temporal eddy-current variations in a model cryostat/gradient pair.

In this work we explore the possibility of including predicted eddy currents in the design process of the gradient coil. Transient eddy currents induced within a realistic cryostat vessel during the pulsing of gradient coils can be applied constructively together with the gradient currents that generate them to obtain a homogeneous gradient in the imaging volume with a desired temporal variation. This can be achieved by simultaneously tailoring the spatial distribution and temporal preemphasis of the gradient coil current to control the effects of eddy currents.

Although this approach could be applied to any known gradient coil and cryostat geometry, for the purposes this study it is constrained to actively shielded and unshielded, symmetric, *z*-axis gradient coils. The simplicity of the 2D problem means that it requires less computational effort than the optimization of a transverse gradient coil with eddy currents.

In order to assist in the computation of the transient eddy currents within a realistic cryostat geometry during the optimization of the longitudinal gradient coils, a low-

School of Information Technology and Electric Engineering, University of Queensland, Brisbane, Australia.

Grant sponsor: Australian Research Council.

*Correspondence to: Professor Stuart Crozier, School of Information Technology and Electrical Engineering, University of Queensland, St. Lucia, Brisbane, Qld 4072, Australia. E-mail stuart@itee.uq.edu.au

Received 28 June 2006; revised 30 January 2007; accepted 21 February 2007.

DOI 10.1002/mrm.21243
Published online in Wiley InterScience (www.interscience.wiley.com).

frequency 2D axial-symmetric finite-difference time-domain (FDTD) method based on the total-field scattered-field (TFSF) (14) technique was performed and verified with the commercially available software package FEMLAB. The application of the TFSF-FDTD approach in calculating the gradient-induced eddy currents is a novel feature of the design method.

The results of this study demonstrate that with a suitable temporal preemphasis and the optimized spatial current distribution applied, the multiexponentially decaying eddy currents can be accurately predicted and constructively used to assist in the design of longitudinal gradient coils that generate very uniform and temporally stable gradient fields.

MATERIALS AND METHODS

Longitudinal Gradient Coil Optimization in the Presence of Transient Eddy Currents

The approach outlined in this work considers the transient eddy currents induced in an example cryostat and the corresponding effects in the diameter spherical volume (DSV) region during the optimization of actively shielded/unshielded *z*-gradient coils. To achieve the desired gradient homogeneity with desired temporal variation, both the spatial distribution and temporal preemphasis of the gradient coil current are simultaneously tailored in the presence of the induced temporal eddy currents. It is essential that the spatial distribution and temporal overshoot of the gradient coil current be coupled during the optimization process in order to control the eddy-current effects in both space and time.

Eddy-Current nonoptimized *z*-Gradient Coil and Switching Sequence

The shielded/unshielded *z*-gradient coil can be first preoptimized without the consideration of eddy-current effects using one of the many design schemes available (15). This *z*-gradient coil can then be used as a reference to the eddy-current optimized coil. Alternatively, it is possible to start with an arbitrary current distribution as the initial condition for the optimization of the spatial distribution and temporal preemphasis of the gradient coil current. During this initial stage, it is possible to include any of the conventional optimization constraints and objectives.

The stand-alone *z*-gradient coil is then theoretically placed within a realistic cryostat vessel and the desired gradient switching sequence is applied. In this study the switching sequence is assumed to be trapezoidal and one-half period in duration. However, any continuous switching sequence type can be used, and more excitation cycles can be included if required.

Computation of the Primary and Secondary Magnetic Fields

This section describes a new and efficient numerical method for the computation of eddy currents in MRI conductors (first within the cryostat). The main purpose of this proposed tool is to assist in the rapid optimization of *z*-gradient coils in the presence of induced transient eddy currents. Pulsing of the gradient coil current generates a time-varying primary magnetic field while at the same time eddy currents are induced in nearby conductors, which leads to formation of the time-varying secondary magnetic field. The primary magnetic field can be computed using the Biot-Savart method. However, the computation of the secondary magnetic field with analytical solutions is not always mathematically straightforward, especially when the eddy currents are produced in geometrically complex conducting structures, such as a cryostat. Numerical schemes such as the FDTD and finite element (FE) techniques are more suitable in these circumstances, provided that repetitive computations of the generated eddy currents are sufficiently rapid during the optimization of the gradient coil.

Consequently, we extend our recent work on the low-frequency FDTD method in cylindrical coordinates (11,12) and improve the scheme by including the TFSF methodology (14). With the TFSF-FDTD scheme in place, the region of interest (ROI, i.e., the cryostat vessel) is enclosed by four boundaries (Eq. [8]) to which the electromagnetic (EM) fields (i.e., the $\bar{H}_r$, $\bar{H}_z$, and $\bar{E}_\varphi$ field components in Eqs. [4]–[7]) from the gradient coil are propagated analytically using elliptic integrals for radial and axial magnetic and azimuthal electric field components (16). The TFSF boundaries mimic the distant gradient coil and act as artificial near-field sources. During FDTD field updating, the EM fields emerge from the TFSF boundaries, propagate into free space, and are incident on the cryostat vessel, from which they are then partially reflected and partially transmitted. The region enclosed by the TFSF boundaries is termed the "total field" region in which both incident and scattered fields exist, whereas the region surrounding the TFSF boundaries contains only scattered fields and is therefore called the "scattered field" region. The TFSF-FDTD computational domain is terminated in a cylindrical split-version perfectly matched layer (PML), absorbing boundary condition (ABC), and perfect electrical conductor (PEC), which artificially truncate/absorb the scattered fields (11,12). The application of the TFSF-FDTD method to the longitudinal gradient coil/cryostat vessel model is shown in Fig. 1.

With the TFSF formulation, only the conductor and a small region of air neighboring the conductor need to be discretized. In this way the computational burden associated with the redundant evaluation of the EM fields in free space encircled by the cylindrical gradient coils can be appreciably minimized. By employing the TFSF technique, we were able to accelerate the FDTD method by a factor of around 6. This computational speed-up is essential during the optimization and prototyping of the gradient coil in the presence of transient eddy currents. Briefly, the central-difference method is applied to the Maxwell's curl equations in 2D axial-symmetric cylindrical coordinates to obtain a set of general FDTD update formulations for the fields inside the conductor (here the cryostat vessel) and surrounding medium (14):

$$H_r|_{i,k+1/2}^{n+1/2} = H_r|_{i,k+1/2}^{n-1/2} + \frac{\Delta t}{\mu}\left(\frac{E_\varphi|_{i,k+1}^{n} - E_\varphi|_{i,k}^{n}}{\Delta z}\right) \qquad [1]$$

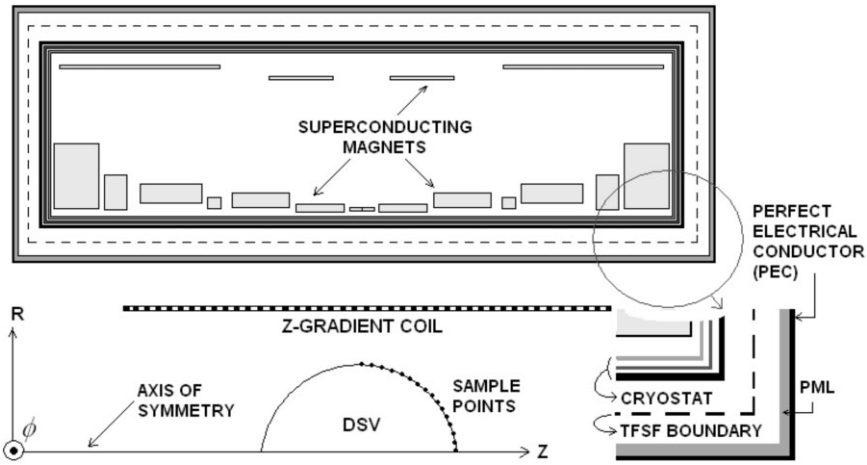

FIG. 1. MRI system setup showing the *z*-gradient coil and the TFSF boundary enclosing the cryostat vessel. The PEC encloses the TFSF-FDTD computational domain.

$$H_z\big|_{1+1/2,k}^{n+1/2} = H_z\big|_{i+1/2,k}^{n-1/2} - \frac{\Delta t}{\mu r_{i+1/2}}\left(\frac{r_{i+1}E_\varphi\big|_{i+1,k}^{n} - r_i E_\varphi\big|_{i,k}^{n}}{\Delta r}\right) \quad [2]$$

$$E_\varphi\big|_{i,k}^{n+1} = \left(\frac{2\varepsilon - \sigma\Delta t}{2\varepsilon + \sigma\Delta t}\right) E_\varphi\big|_{i,k}^{n} + \left(\frac{2\Delta t}{2\varepsilon + \sigma\Delta t}\right) \times \left(\frac{H_r\big|_{i,k+1/2}^{n+1/2} - H_r\big|_{i,k-1/2}^{n+1/2}}{\Delta z} - \frac{H_z\big|_{i+1/2,k}^{n+1/2} - H_z\big|_{i-1/2,k}^{n+1/2}}{\Delta r}\right) \quad [3]$$

Where the transient TFSF boundary conditions are given by:

BOTTOM INTERFACE:

$$H_r\big|_{i,k_0-1/2}^{n+1/2} = \{H_r\big|_{i,k_0-1/2}^{n+1/2}\}_{[1]} + \left(\frac{\Delta t\bar{E}_\varphi\big|_{i,k_0}^{n}}{\mu\Delta z}\right) \quad E_\varphi\big|_{i,k_0}^{n+1} = \{E_\phi\big|_{i,k_0}^{n+1}\}_{[3]} - \left(\frac{2\Delta t\bar{H}_r\big|_{i,k_0-1/2}^{n+1/2}}{2\varepsilon\Delta z + \sigma\Delta t\Delta z}\right) \quad [4]$$

TOP INTERFACE:

$$H_r\big|_{i,k_1+1/2}^{n+1/2} = \{H_r\big|_{i,k_1+1/2}^{n+1/2}\}_{[1]} - \left(\frac{\Delta t\bar{E}_\varphi\big|_{i,k_1}^{n}}{\mu\Delta z}\right) \quad E_\phi\big|_{i,k_1}^{n+1} = \{E_\phi\big|_{i,k_1}^{n+1}\}_{[3]} + \left(\frac{2\Delta t\bar{H}_r\big|_{r,k_1+1/2}^{n+1/2}}{2\varepsilon\Delta z + \sigma\Delta t\Delta z}\right) \quad [5]$$

LEFT INTERFACE:

$$H_z\big|_{i_0-1/2,k}^{n+1/2} = \{H_z\big|_{i_0-1/2,k}^{n+1/2}\}_{[2]} - \left(\frac{r_{i_0}\Delta t\bar{E}_\varphi\big|_{i_0,k}^{n}}{r_{i_0-1/2}\mu\Delta r}\right) \quad E_\phi\big|_{i_0,k}^{n+1} = \{E_\phi\big|_{i_0,k}^{n+1}\}_{[3]} + \left(\frac{2\Delta t\bar{H}_z\big|_{i_0-1/2,k}^{n+1/2}}{2\varepsilon\Delta r + \sigma\Delta t\Delta r}\right) \quad [6]$$

RIGHT INTERFACE:

$$H_z\big|_{i_1+1/2,k}^{n+1/2} = \{H_z\big|_{i_1+1/2,k}^{n+1/2}\}_{[2]} + \left(\frac{r_{i_1}\Delta t\bar{E}_\varphi\big|_{i_1,k}^{n}}{r_{i_1+1/2}\mu\Delta r}\right) \quad E_\phi\big|_{i_1,k}^{n+1} = \{E_\phi\big|_{i_1,k}^{n+1}\}_{[3]} - \left(\frac{2\Delta t\bar{H}_z\big|_{i_1+1/2,k}^{n+1/2}}{2\varepsilon\Delta r + \sigma\Delta t\Delta r}\right) \quad [7]$$

where H_r and H_z denote the radial and axial components of the magnetic field in [A/m] and E_φ is the azimuthal electric field in [V/m]. The superscript n relates to the time in units of Δt, and subscripts i and k relate to the spatial position in units of Δr and Δz, respectively. The permeability $\mu(r, z)$, permittivity $\varepsilon(r, z)$, and material conductivity $\sigma(r, z)$ are defined at the center of the Yee cell. Variables r_i, $r_{i+1/2}$, and r_{i+1} are the radial coordinates in [m]. The TFSF boundary is assumed to be a rectangular box with the following discrete limits:

$$i = \{i \in N | i_0 \le i < i_1\} \wedge k = \{k \in N | k_0 \le k < k_1\}. \quad [8]$$

The first terms in curly brackets on the right-hand side (RHS) of Eqs. [4]–[7] are the generic time-stepping operations as expressed in Eqs. [1]–[3]. The second terms on the RHS of Eqs. [4]–[7] are the added incident-wave terms that arise from the artificial near-field sources present on the TFSF boundaries. In general, the first terms on the RHS of Eqs. [4]–[7] are implemented first, after which the incident-wave terms are added. The temporal variation in the fields due to the gradient coil (i.e., preemphasized trapezoidal excitation) is inherently introduced by the second terms on the RHS of Eqs. [4]–[7]. A comprehensive treatment of the TFSF theory, from which Eqs. [4]–[7] are derived, is given in Ref. 14.

FDTD is a popular scheme for the solution of high-frequency problems, due to its simplicity and efficiency in wave models. At low frequencies, however, Maxwell's equations lose their symmetry, as the conducting current is many orders of magnitude larger than the displacement current. Similarly to our recent work (12), the standard FDTD scheme can be adapted to low frequencies by appropriate linear scaling of certain physical constants. One way to achieve the adaptation is to scale up the permittivity of free space ε_0 and to leave the permeability μ_0 unchanged. The downscaled speed of light constant c_α is then given by:

$$c_\alpha = \frac{1}{\sqrt{\mu_0(\alpha\varepsilon_0)}} = \frac{1}{\sqrt{\mu_0\varepsilon_\alpha}} \quad [9]$$

where α is a dimensionless scaling factor, c_α is the scaled speed of the light constant [in ms^{-1}], μ_0 is the permeability

of free space [$4\pi \cdot 10^{-7} WbA^{-1}m^{-1}$], ε_0 is the permittivity of free space [$8.8542 \cdot 10^{-12} C^2N^{-1}m^{-2}$] and ε_α is the scaled free space permittivity. The modification directly implies an alternation of the free space impedance, and if the source is specified in terms of the electric field amplitude, the magnetic field will be scaled up by a factor of $\sqrt{\alpha}$. However, if a magnetic field source is specified, the electric field will be scaled down by the same factor. In this study the current source is in terms of the electric field, which necessitates downscaling of the magnetic field results by the aforementioned factor at the end of simulation.

The TFSF-FDTD formulation allows direct and efficient numerical computation of eddy currents induced within the conducting region (the cryostat vessel) during pulsing of a magnetic field gradient. Using the superposition theorem, the secondary transient magnetic field in the imaging volume of the gradient coil can be obtained by numerical integration, provided the eddy-current electric field in the conducting region is known. First the eddy current within every Yee cell of the conducting region $I_{\varphi,eddy} = \sigma E_{\varphi,eddy} \Delta r \Delta z$ is computed, followed by numerical integration of the induced eddy current to obtain the corresponding secondary axial magnetic field in the imaging volume.

Verification of the Computational Method

The low-frequency, cylindrical TFSF-FDTD formulation was coded in C and verified on a numerical model using the FE software package FEMLAB©. An unshielded 20-turn symmetric *z*-gradient was designed to have a diameter of 710 mm with axial coil coordinates detailed in Table 1. The gradient coil generates a DSV (here $< 5\%$ peak-to-peak (pp) gradient uniformity error) with radial and axial diameters of 0.45 m.

A trapezoidal current density with the maximum amplitude of 1 A/m^2 at a frequency and rise time of 1 *kHz* and 100 μs, respectively, was used to excite the coil. The gradient coil is placed in a realistic cylindrical cryostat vessel consisting of stainless steel and two aluminum radiation shield layers. Table 2 lists the physical properties of the cryostat vessel walls. The total length of the cryostat was assumed to be 1.4 m.

With radial and axial Yee cell sizes of 0.25 mm and 7 mm, respectively, the cryostat bore was suitably discretized to capture the spatial exponential decay (skin effect) of propagating waves as they penetrated the conducting walls. The 2D computational problem contained 61600 FDTD cells.

An identical model was implemented in FEMLAB as the 2D axial symmetric problem with the quasistatic solver for transient azimuthal currents. The gradient coil and the cryostat vessel were enclosed in a large rectangular air domain, where axial symmetric and magnetic insulation boundary conditions were appropriately applied to the borders of that domain. The dielectric properties of the cryostat vessel were then input according to Table 2, and the gradient coil current density of 1 A/m^2 was amplitude-modulated by the predefined trapezoidal function with the parameters identical to the TFSF-FDTD model setup. The computational space was then unevenly meshed with a total of 31560 FE nodes. The transient simulation was carried out for one excitation period with temporal resolution of 10 μs. The relative and absolute temporal tolerances were set to 1 *ps*. The direct UMFPACK solver was then used to solve the transient problem, after which the results were postprocessed.

Table 1
Gradient Coil Parameters

Axial coil coordinates (± mm)									
139	322	382	449	460	522	527	539	581	590

Table 2
Cryostat Vessel Properties

#	Material	Conductivity (MS/m)	Thickness (mm)	Inner radius (mm)
1	Stainless steel	~ 1.05 @ 300 K	5	450
2	Aluminum	~ 100 @ 80 K	3	465
3	Aluminum	~ 500 @ 4.3 K	6	478

z-Gradient Discrete Optimization Approach

To compensate for multiexponentially decaying secondary magnetic fields, current preemphasis is achieved using a series of three exponential functions with characteristic RC-time constants and amplitudes that are readily adjustable on a preemphasis network of the MR imager. The use of only three exponential terms is sufficient in this case. However, more exponential terms can be used if convergence of the optimization is inadequate.

The time-varying primary B_z^p (due to gradient coil) and secondary B_z^s (due to eddy currents) axial magnetic fields add vectorially to produce the resulting magnetic field gradient, which must be homogeneous to 5%pp and have a pure trapezoidal temporal variation in the imaging volume. Commonly, the secondary magnetic field due to eddy currents distorts the spatial and temporal qualities of the gradient field. To compensate for these disturbances, the gradient-coil current distribution and temporal variation are optimized so that gradient-induced eddy currents will generate secondary magnetic fields that will add to the primary magnetic fields and produce a total spatially homogeneous and temporally stable magnetic field gradient in the imaging volume. To achieve this goal, a number N of temporal sample points equally spaced in time are used to discretize the switching sequence (i.e., the preemphasized trapezoidal waveform). The time spacing between adjacent temporal sample points is related to the time increment $\Delta\tau$ [s]. The n^{th}-temporal sample point can be found at time t_n[s]:

$$t_n = n\Delta\tau \quad \text{where } n \in \{1 \ldots N\} \qquad [10]$$

At every temporal sample point, the primary B_z^p and secondary B_z^s axial magnetic fields are computed at M spatial sample points evenly distributed on the upper quarter of the DSV periphery, as illustrated in Fig. 1. The distribution of spatial sample points was:

$$z_m = R_z - \Delta Z(m-1)$$

$$r_m = R_r \sin\left(a \cos\left(\frac{z_m}{R_2}\right)\right) \quad \text{where } m \in \{1 \ldots M\} \quad [11]$$

where r_m and z_m denote the radial and axial 2D axial-symmetric cylindrical coordinates of the spatial sample points in [m], respectively; ΔZ is the fixed axial distance between adjacent sample points in [m]; R_r and R_z are the radial and axial DSV semi-axes in [m]; and m is the index of the spatial sample point.

The primary magnetic field due to the gradient coil is computed with the Biot-Savart method and varies in time in accordance with the preemphasized gradient coil current excitation. The secondary magnetic field due to the eddy currents induced in the cryostat is calculated using the TFSF-FDTD method described previously, and its time-space behavior is a function of the time-dependent primary magnetic field. Then the total time-varying axial magnetic field $B_{z^{tot}}$ is given by:

$$B_z^{tot}(r_m, z_m, t_n) = B_z^p(r_m, z_m, t_n) + B_z^s(r_m, z_m, t_n) \quad [12]$$

Here the term $B_z^{tot}(r_m, z_m, t_n)$ indicates that the total axial magnetic field is calculated at a spatial sample point with the radial and axial coordinates r_m and z_m, at time t_n. Based on the total magnetic field, m total axial magnetic field gradient values G_z^{tot} at every temporal sample point can be derived based on the following difference equation:

$$G_z^{tot}(r_m, z_m, t_n) = \frac{B_z^{tot}(r_{m+1}, z_{m+1}, t_n) - B_z^{tot}(r_m, z_m, t_n)}{\Delta Z} \quad [13]$$

with $m \in \{1 \ldots M - 1\}$.

The eddy-current-distorted total gradient field on the periphery of the imaging volume will always contain spatial positions where gradient magnitudes are larger and/or smaller than the desired gradient field over time. Depending on the spatial distribution of eddy currents in the cryostat vessel, there will be one spatial sample point where a maximum gradient field waveform is traced in time and usually another spatial different point with a minimum waveform trace. The prime purpose of this algorithm is to minimize the divergence between these two extremes and the closest desired gradient field over time.

Therefore, for every temporal sample point, the maximum and minimum total magnetic field gradient values are computed based on the dataset of total gradient values on M spatial sample points:

$$G_{z,\max}^{tot}(t_n) = \max(G_z^{tot}(r_m, z_m, t_n)) \wedge G_{z,\min}^{tot}(t_n) = \min(G_z^{tot}(r_m, z_m, z_m, t_n)) \quad [14]$$

Here $G_{z,\max}^{tot}(t_n)$ and $G_{z,\min}^{tot}(t_n)$ signify the maximum and minimum total gradient field waveform traces over time, respectively. These waveforms contain the eddy-current-induced distortions.

To obtain the closest desired gradient of pure trapezoidal waveform and with the largest possible magnitude (i.e., for maximum gradient efficiency), we calculate the maximum values of $G_{z,\max}^{tot}(t_n)$ and $G_{z,\min}^{tot}(t_n)$:

$$G_{z,\max 1} = \max(G_{z,\max}^{tot}(t_n)) \wedge G_{z,\max 2} = \max(G_{z,\min}^{tot}(t_n)) \quad [15]$$

The average of $G_{z,\max 1}$ and $G_{z,\max 2}$ is computed and the resulting magnitude is multiplied by the unit trapezoidal response (discretized by N temporal sample points):

$$G_{z,CD}(t_n) = \left(\frac{G_{z,\max 1} + G_{z,\max 2}}{2}\right) \cdot \Xi(t_n) \quad [16]$$

where $\Xi(t_n)$ is the discretized unit trapezoidal response and $G_{z,CD}(t_n)$ is the closest desired (CD) magnetic field gradient over time. Figure 2 visualizes the algorithm approach in generating the closest desired gradient.

The next important step is to minimize the difference between $G_{z,CD}(t_n)$ and the field extremes $G_{z,\max}^{tot}(t_n)$ and $G_{z,\min}^{tot}(t_n)$. This is achieved by simultaneous optimization of gradient coil current distribution and temporal current preemphasis excitation used in driving the coil. Due to the simplicity of the gradient coil, a discrete current distribution was assumed and axial coil positions were varied in the presence of eddy currents. However, analytical expressions of the continuous current distribution can be also optimized. In the preemphasis excitation, three amplitude and three RC-time constant coefficients were varied. In this work we successfully employed the nonlinear Levenberg-Marquardt (LM) least-square optimization algorithm to minimize the following objective function:

$$\psi = \sum_{n=1}^{N} \max\left[\left(\frac{G_{z,\max}^{tot}(t_n) - G_{z,CD}(t_n)}{G_{z,CD}(t_n)}\right)^2, \left(\frac{G_{z,\min}^{tot}(t_n) - G_{z,CD}(t_n)}{G_{z,CD}(t_n)}\right)^2\right] \quad [17]$$

The objective function ψ is satisfied when its value at every temporal sample point is less than 5%pp (the industry standard).

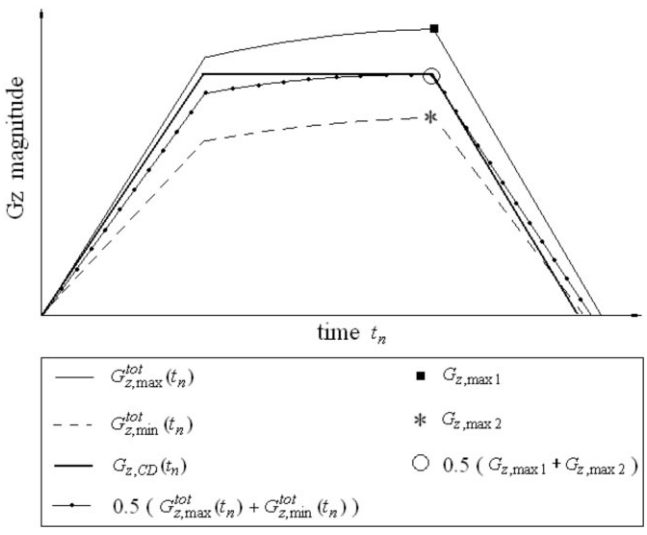

FIG. 2. Illustration of the algorithm approach for deriving the closest desired gradient over time, $G_{z,CD}(t_n)$.

Table 3
Nonoptimized vs. Optimized Unshielded Z-Gradients

	Axial coil coordinates (± mm)									
Coil A										
Nonoptimized	140	340	345	355	425	455	463	480	485	500
Optimized	140	335	340	353	425	494	463	480	485	500
Change Δz	0	−5	−5	−2	0	+39	0	0	0	0
Coil B										
Nonoptimized	139	322	382	449	460	522	527	539	581	590
Optimized	127	310	313	327	471	477	494	522	531	533
Change Δz	−12	−12	−69	−122	−11	−45	−33	−17	−50	+57

Single-Layer Longitudinal Gradient Optimization Example

A shorter version of the *z*-gradient coil from Table 1, with an overall length of 1 m, was first optimized without the presence of eddy currents using the LM-optimization method. It was assumed that the coil is made of circular copper wires with 3-mm diameter. Rectangular copper wires could have been also used. Furthermore, it was assumed that the target field uniformity, gradient efficiency, adequate gradient, and DSV geometry are the only applicable optimization constraints. The gradient coil was then positioned inside the three-layer cryostat vessel detailed in Table 2, and a maximum current of 1A was pulsed trapezoidally through the gradient coil at a frequency of 1 kHz with 100 μs rise time. For illustration purposes, only one-half of the trapezoidal period was discretized with $N = 50$ temporal sample points and used in all optimization calculations. The DSV size constraint was assumed to be identical to the stand-alone single-layer *z*-gradient coil (i.e., 0.45 × 0.45 m). Due to the model symmetry, only one-quarter of the DSV periphery was discretized by $M = 15$ spatial sample points. For maximum performance with eddy currents, it was necessary to simultaneously reoptimize the *z*-gradient coil wire positions and the preemphasis excitation. The optimization was terminated when the maximum deviation of less than 5%pp from the desired gradient over time was achieved.

Study of Different Gradient Rise Times

It is well known that eddy currents depend not only on the gradient coil/cryostat geometry and intrinsic properties, but also on the gradient current rise time and switching sequence employed (17). It is therefore essential to study different excitations and the resulting implications for eddy-current spatial and temporal behavior to ensure that the eddy-current optimized gradient design is stable. In this study the axial coil positions of the eddy-current optimized coil A (Table 3) were assumed to be constant, and thus only the current overshoot was tailored to account for the rise-time-specific eddy currents induced in the cryostat bore. Four simulations were conducted with rise times of 150, 200, 250, and 300 μs, respectively.

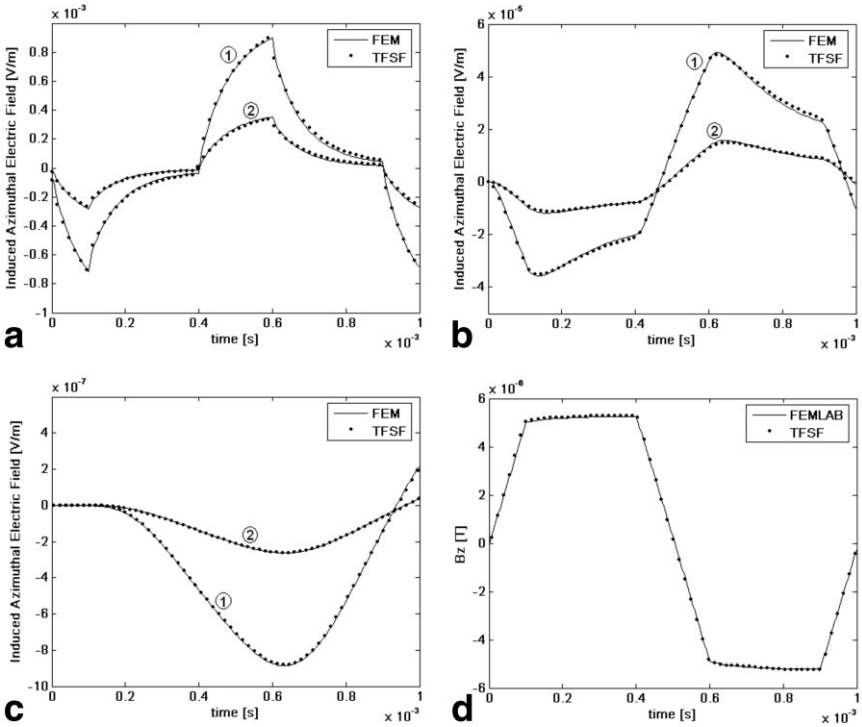

FIG. 3. Transient validation results: (**a**) first wall (stainless steel), (**b**) second wall (aluminum), and (**c**) third wall (aluminum), where waveforms 1 and 2 are spatial points taken at the inner surface 0.21 m and 0.07 m axially from the center of axis of symmetry, respectively. Subplot **d** represents the secondary axial magnetic flux density due to the whole cryostat vessel at $R = 0$; $Z = 0.225$ m.

Actively Shielded Longitudinal Gradient Optimization Example

In this part of the study an actively shielded stand-alone symmetric *z*-gradient coil was optimized without the consideration of eddy currents. The gradient-coil optimization aims were to minimize the leakage fields at the first eddy-current source (inner cryostat wall), maximize the gradient efficiency, and obtain at most 5%pp gradient uniformity in a 500 × 560 mm working volume. The shielding effectiveness of the actively shielded gradient coil is computed at 100 spatial points equally spaced along the *z*-axis ($z = -1...1m$) at radial distances of 0.45 m (first eddy-current source) and 0.5 m (inner surface of the first superconducting magnets). The inner and outer coil diameters were fixed at 700 mm and 800 mm, respectively. It was assumed that this coil is also made of circular copper wires with 3-mm diameter. During the optimization procedure, the axial half lengths of the primary and secondary layers were constrained to 480 mm and 530 mm, respectively.

The eddy-current nonoptimized, actively-shielded *z*-gradient coil was then situated inside the cryostat vessel as detailed in Table 1, and a maximum current of 1A was pulsed trapezoidally through the gradient coil at a frequency of 1 kHz with $100\mu s$ rise time. A spatial and temporal discretization ($N = 50$, $M = 15$) identical to the single-layer *z*-gradient coil optimization was used. The gradient current overshoot and axial coil positions in both the primary and secondary gradient layers were then optimized to account for the presence of secondary magnetic fields in the imaging volume. The leakage fields were also minimized during the same optimization process.

RESULTS

Verification of the Computational Method

On a dual XEON 3.6GHz/4GB RAM PC platform and with a scaling factor of $\alpha = 9 \cdot 10^{10}$, the TFSF-FDTD method

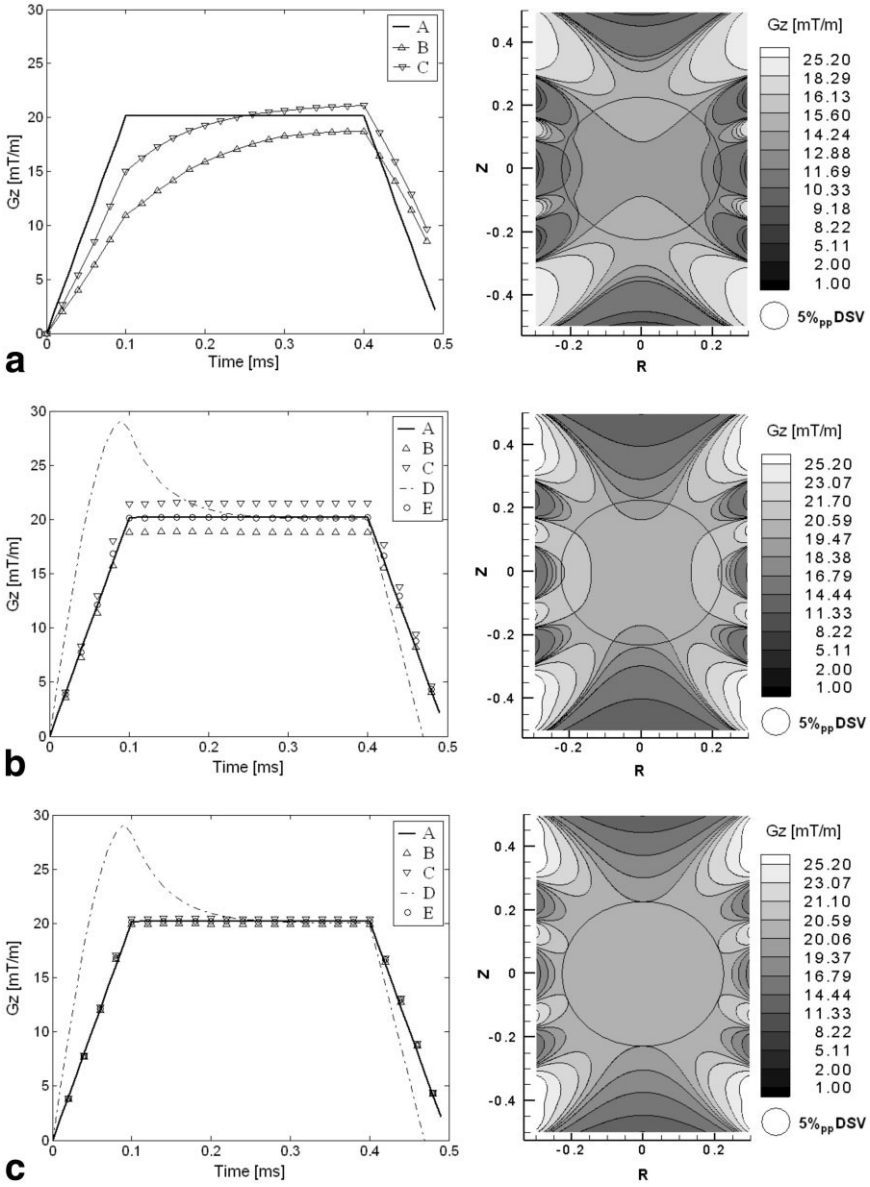

FIG. 4. Gradient field vs. time due to the single-layer longitudinal gradient coil (here coil A) at 500A transport current and eddy currents induced in the cryostat vessel (left), and gradient uniformity snapshot at 0.11 ms after the start of the gradient waveform (right). The gradient waveforms (left) show the (**A**) closest desired gradient $G_{z,CD}(t_n)$, (**B**) minimum total gradient $G^{tot}_{z,\min}(t_n)$, (**C**) maximum total gradient $G^{tot}_{z,\max}(t_n)$, (**D**) sketch of scaled preemphasized current excitation. and (**E**) total gradient in the center of the DSV over time $G^{tot}_{z,center}(t_n)$. The subplots illustrate (**a**) a spatially and temporally nonoptimized coil, (**b**) a spatially nonoptimized coil driven with optimal preemphasis, and (**c**) a spatially optimized gradient coil driven with optimal preemphasis.

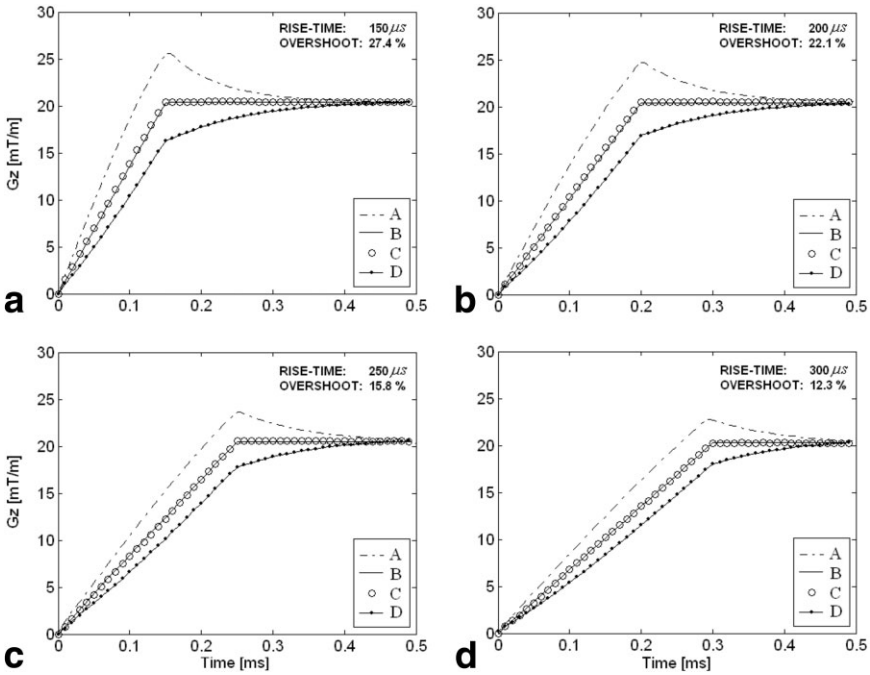

FIG. 5. Gradient field vs. time due to single-layer longitudinal gradient coil (here coil A) at 500A transport current and eddy currents induced in the cryostat vessel, where the axial coil positions have been fixed and only the rise-time-specific preemphasis has been tailored: (**a**) sketch of scaled preemphasized current excitation $\Xi(t_n)$, (**b**) closest desired gradient uniformity over time $G_{z,CD}(t_n)$, (**c**) optimized gradient uniformity over time where eddy-current effects have been taken into account, and (**d**) gradient uniformity over time degraded due to eddy currents (with optimal preemphasis not applied).

required around 8 s to obtain the transient field result for one period of the trapezoidal sequence. The model problem was that described in the Materials and Methods section under "Verification." In contrast, the commercial software package FEMLAB took around 34 s on the same platform to solve the identical problem. Although the number of nodes in the FE setup was about twice as large as the number of cells used in the FDTD method, the TFSF-FDTD formulation was around four times faster than the FE method.

Figure 3 compares the transient, azimuthal eddy-current electric fields at different locations within the cryostat vessel between the TFSF-FDTD and FEMLAB simulations. The results are in good agreement.

Single-Layer Gradient Optimization Results

On the dual XEON PC platform, the single-layer *z*-gradient coil eddy-current-based optimization consumed around 28 min of CPU time and 6.3 MB of memory. Table 3 lists the axial coordinates of the eddy-current nonoptimized and optimized gradient coils, indicating the changes in the axial positions required to accommodate the eddy-current fields. The terms "coil A" and "coil B" in Table 3 signify the short and long single-layer *z*-gradient coils.

Figure 4a (left) illustrates the deviation of the gradient uniformity from the target gradient over time for an eddy-current nonoptimized coil (Table 3, coil A—nonoptimized) in the presence of eddy currents. The results illustrated in Fig. 4b (left) indicate that if only the optimal preemphasis is applied to the eddy-current nonoptimized coil A, the target field uniformity cannot be guaranteed. Figure 4c (left) shows that with simultaneous application of optimal current preemphasis and appropriate variation in axial coil positions (Table 3, coil A, optimized), the target gradient uniformity (<5% pp gradient uniformity error) over time can be obtained. The scaled version of the required preemphasized current excitation is also illustrated in the same plot. Figure 4 (right) depicts the associated worst-case gradient uniformity snapshots within the working volume at 500A transport current for all three aforementioned cases at 0.11 ms after the start of the gradient waveform. The same optimization procedure was applied to the longer *z*-gradient coil from Table 1 with similar CPU time and memory requirements, and analo-

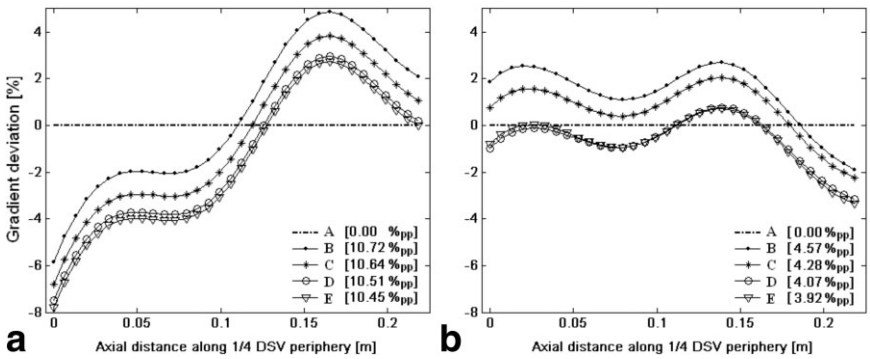

FIG. 6. Spatial gradient deviation from the target gradient along the axial coordinates of the upper-quarter DSV periphery at 0.11 ms: (**a**) spatially nonoptimized axial coil positions of coil A and optimal current preemphasis (Fig. 5), (**b**) spatially optimized axial coil positions of coil A and optimal current preemphasis (Fig. 5), (**A**) target gradient uniformity, and gradient uniformity at (**B**) 150 μs, (**C**) 200 μs, (**D**) 250 μs, and (**E**) 300 μs rise time, respectively.

Table 4
Nonoptimized vs. Optimized Actively Shielded *z*-Gradients

	Axial coil coordinates (± mm)														
First layer															
Nonoptimized	98	196	221	282	362	395	411	419	452	455	458	461	464	467	480
Optimized	95	193	223	286	362	392	410	415	445	449	455	459	464	472	479
Change Δz	−3	−3	+2	+4	0	−3	−1	−4	−7	−6	−3	−2	0	+5	−1
Second layer															
Nonoptimized	115		198		269		341		380		416		434		463		482		526
Optimized	112		200		278		339		380		413		433		467		483		528
Change Δz	−3		+2		+9		−2		0		−3		−1		+4		+1		+2

gous results to Fig. 4 were obtained (not shown). By incorporating the eddy currents in the design process, it may be possible to shape larger DSV regions than by using the single-layer gradient coil alone.

Gradient Rise Time Results

In Fig. 5 the axial coil positions of the eddy-current optimized coil A (Table 3) were assumed to be constant and only the current overshoot was tailored to account for the rise-time-specific eddy-current temporal effects generated in the imaging volume. As expected, the slower the gradient current rise time, the smaller the temporal eddy-current distortions and hence less preemphasis is required. Increasing the current rise time from 150 to 300 μs decreased the required overshoot in the gradient-coil current by a factor of more than 2.2. Figure 6 illustrates snapshots of the spatial gradient deviation from the target field uniformity along the axial coordinates of one-quarter DSV periphery (0.45 × 0.45 m) for the different rise-time conditions at 0.11 ms.

Figure 6a shows the spatial gradient deviation assuming the fixed, eddy-current nonoptimized coil A (Table 3) and the rise-time-dependent overshoots from Fig. 6, while Fig. 6b) illustrates results for the eddy-current optimized coil A. The preemphasized, spatially nonoptimized gradient coil caused more than 10%pp gradient deviation from the target field uniformity under all rise-time conditions that were studied (Fig. 6a). Other gradient coils could potentially generate more deviation under these circumstances. However, in the case of the preemphasized, spatially optimized gradient coil, the gradient deviation was below 5%pp for all rise times (Fig. 6b). These results illustrate that a priori optimization of spatial current distribution is advantageous for achieving the target field uniformity and ensuring stability. In addition, Fig. 6 illustrates that in both cases (subplots a and b), the spatial gradient deviation tends to decrease slightly as the rise time increases.

Actively Shielded Gradient Optimization Results

Using the same computing platform detailed in "Verification of the Computational Method" above, it took around 52 min to obtain the solution for the actively shielded case. Table 4 lists the axial coordinates for the nonoptimized and optimized gradient coils, indicating the changes in axial positions required in the presence of eddy currents. Figure 7 illustrates the shielding performance of the stand-alone actively shielded *z*-gradient assembly at radial distances of 0.45 m (first eddy-current source) and 0.5 m (inner surface of first superconducting magnets). It can be observed that higher-frequency spatial oscillations in the eddy-current source are present when the actively shielded gradient coil is placed within the vicinity of the cryostat bore.

Figure 8 shows the gradient uniformity within the working volume at 500A transport current for nonoptimized (a) and optimized (b) case of the actively shielded gradient coil at 0.11 ms after the start of the gradient waveform. Figure 8a illustrates that active shielding does not guarantee the target field uniformity. By applying the optimization method, the target field uniformity can be obtained (Fig. 8b).

Figure 9 shows the deviation of the gradient uniformity from the desired gradient over time and the optimized solution that follows the prescribed trapezoidal pattern with less than 5%pp deviation from desired gradient field. Also illustrated is the scaled version of the current preemphasis.

Figure 10 illustrates the eddy-current density at the inner surface of three cryostat walls along the *z*-axis vs. time for the nonoptimized and optimized unshielded and actively shielded *z*-gradient coils. The plot shows the effects of preemphasis and perturbed current distribution on the spatial and temporal characteristics of the induced eddy currents.

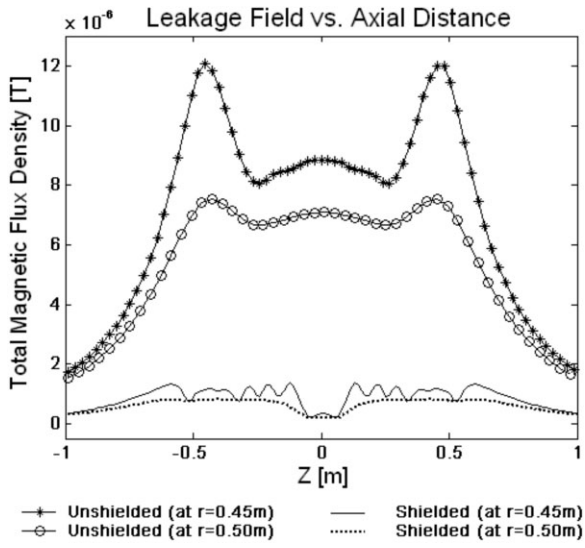

FIG. 7. Shielding characteristics at $r = 0.45m$ (inner surface of cryostat) and $r = 0.50m$ (inner surface of first superconducting main magnet) along the *z*-axis for the actively shielded and unshielded longitudinal gradient coils. The shielding effectiveness $|B_{shielded}/B_{unshielded}|^2$ where $B = \sqrt{B_z^2 + B_r^2}$ (total magnetic flux density) is around 0.012745.

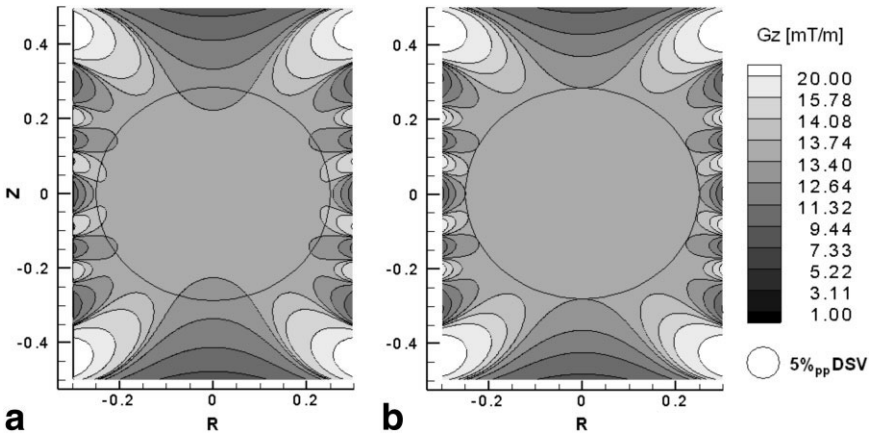

FIG. 8. Gradient uniformity snapshots at 500A transport current at 0.11 ms of trapezoidal excitation due to the (**a**) nonoptimized gradient coil and induced transient eddy currents, and (**b**) spatially and temporally optimized gradient coil and eddy currents. The gradient uniformity in b is preserved during the whole excitation.

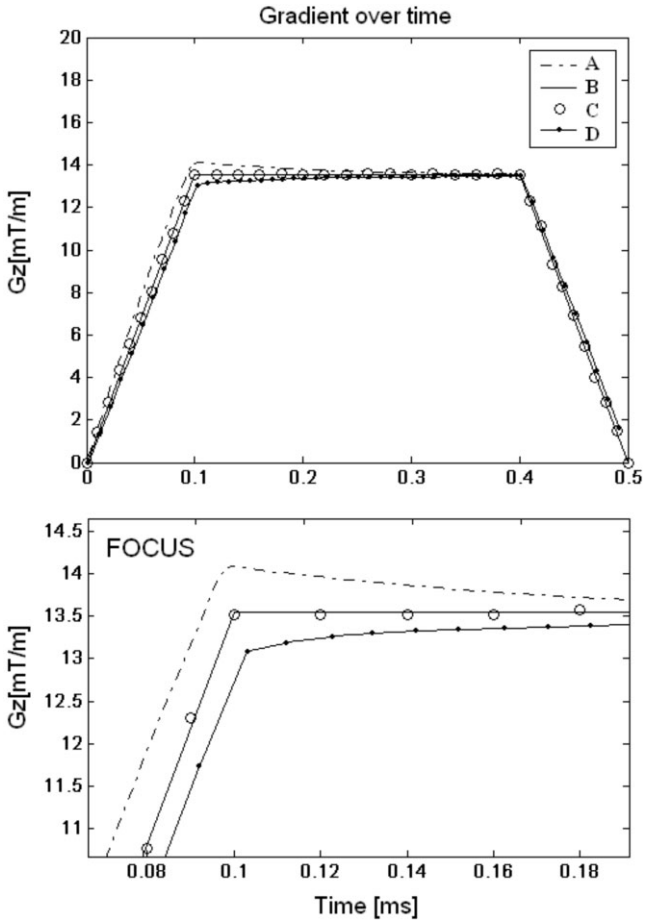

FIG. 9. The gradient field vs. time for actively shielded coil at 500A transport current: (**a**) sketch of scaled preemphasized current excitation, (**b**) closest desired gradient uniformity over time $G_{z,CD}(t_n)$, (**c**) optimized gradient uniformity where eddy currents are taken into account, and (**d**) maximum spatial gradient uniformity degradation over time due to eddy currents (nonoptimized gradient case). Shown below is the focused plot at around 0.1 ms of trapezoidal excitation, illustrating that the optimized gradient uniformity is following the closest desired gradient (e.g., trapezoidal profile).

DISCUSSION

The results obtained in this theoretical study clearly demonstrate the possibility of including predicted transient eddy currents into the design process for shielded and unshielded longitudinal gradient coils. Although this study focused on axial gradients, it certainly seems possible to apply the described method to more general cases (i.e., transverse, planar, and other coil geometries). However, the optimization of 3D gradient systems (i.e., transverse cylindrical coils) could be computationally intensive. This computational burden can be effectively mitigated through parallel computing, which we recently demonstrated for Cartesian and cylindrical systems (18).

A numerical description of the eddy current associated with gradient switching is of significant utility in the MRI field. A robust analysis scheme allows for a more complete design and optimization of gradient coil/cryostat/magnet combinations and gives indicative predictions of the compensation waveforms required (11,12). To assist in the efficient computation of EM fields during gradient switching and thus enable the optimization of *z*-gradient coils in the presence of eddy currents, we extended our recently proposed low-frequency FDTD method by including the TFSF scheme, which effectively accelerates the original computational method. Unlike most analytical formulations, the low-frequency TFSF-FDTD numerical algorithm can be used to compute spatially distributed temporal eddy currents in realistic cryostat vessel geometries and possibly other conducting materials induced by a *z*-gradient coil with almost any continuous switching sequence applied. In a typical experiment, the TFSF boundaries, PEC, and PML layers would be placed around a set of conducting objects of interest, mainly close to the cryostat vessel, and the TFSF-FDTD simulation would be carried out. We note here that we have focused only on the eddy currents induced in the cryostat as they are the main sources of the secondary magnetic fields, and RF-related electrical components (RF shielding and coils) are neglected in this formulation. If all of the conducting MRI components are considered, a domain-decomposition approach can then be utilized. We emphasize also that this efficient TFSF formulation will make the eddy-current evaluations relatively easy to implement for 3D gradient coil designs.

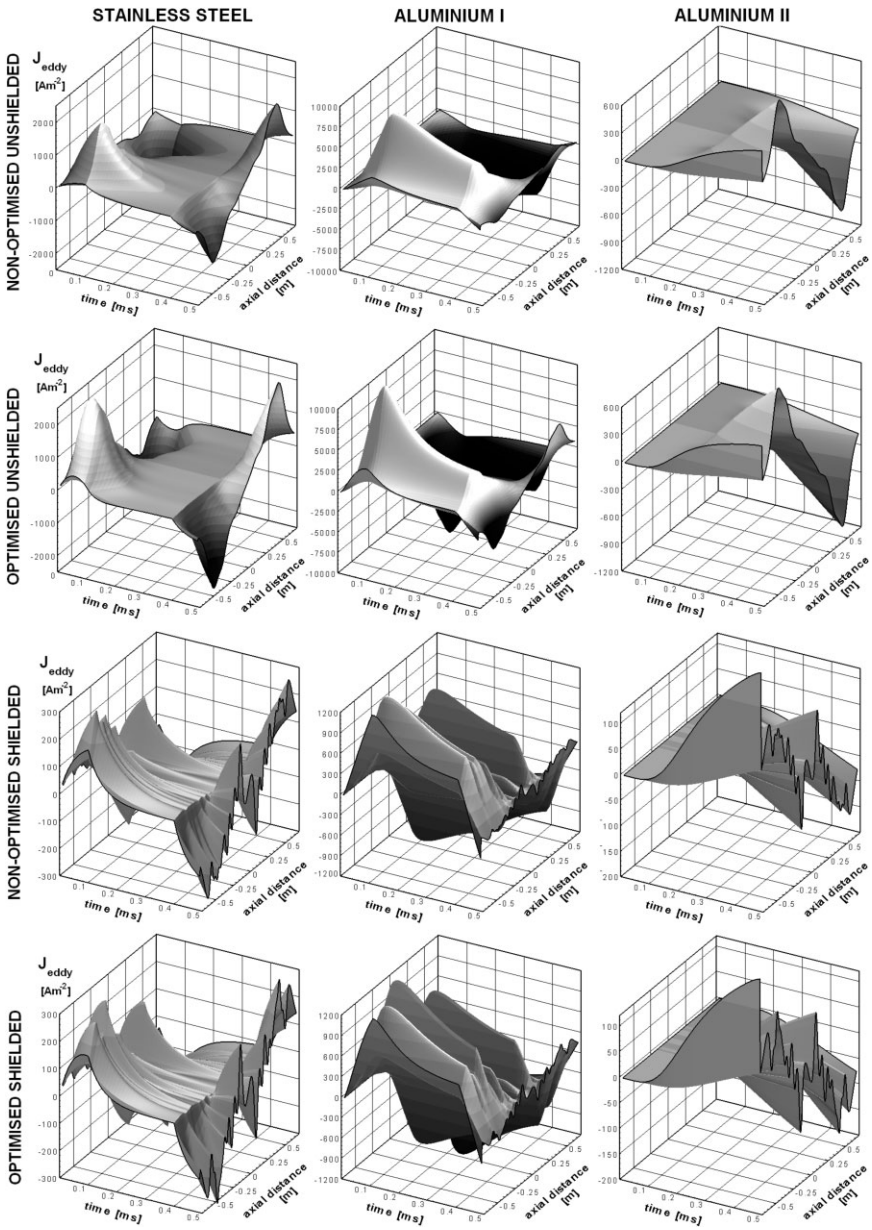

FIG. 10. Eddy-current density along the *z*-axis vs. time at the inner surface of the stainless steel, aluminum I, and aluminum II cryostat walls for the nonoptimized and optimized unshielded (coil A) and actively shielded symmetric *z*-gradient coils at 1A transport current.

In the optimization approach we have assumed that the target field uniformity, adequate gradient and DSV geometry, leakage fields, gradient efficiency and eddy-current spatial and temporal distortions are the only applicable optimization constraints. Obviously, other parameters can be included in the optimization kernel. For instance, during each optimization loop, the total inductance and resistance can be calculated and their implications on gradient switching performance can be included in the model. The approach presented here is somewhat different from traditional methods in that the B_0-shifts due to eddy currents are not separately corrected for, since eddy-current fields are strictly taken into account during the system optimization and B_0-shifts are inherently minimized.

The numerical results obtained in the eddy-current-based single-layer *z*-gradient optimization study promote the possibility of employing the primary gradient layer and the cryostat vessel as the passive shield to generate uniform gradient fields with pure trapezoidal temporal characteristics, provided the single-layer *z*-gradient coil current is both spatially and temporally optimized in the presence of eddy currents. Therefore, depending on the maximum possible performance of the gradient amplifiers/preemphasis unit, it may be possible to remove the active gradient screen and use a suitably designed cryostat vessel as the controlled passive ("natural") shield instead. This could potentially improve the gradient-coil efficiency (since the cryostat is further away from the primary coil than the conventional active shield), minimize the gradient construction costs, and, most importantly, free a significant amount of vital space inside the MRI bore, which could then be used for other purposes. The downsides of this approach include greater field penetration and increased heat load in the cryostat, and the fact that the design optimization is specific to a gradient/cryostat pair. We note that designs in between a shielded and an un-

shielded system are possible using this method; that is, a "lightly" shielded system with high efficiency and good temporal stability and linearity can be obtained.

Based on the results illustrated in Figs. 4–6, the required spatial homogeneity can not be always realized with the current preemphasis alone, and spatial reoptimization of gradient current distribution to account for the secondary fields in the imaging volume is also required for the optimal results. The corrections in wire positions detailed in Tables 3 (single-layer *z*-gradient) and 4 (actively-shielded *z*-gradient) to accommodate for the transient eddy currents are feasible. Clearly, with active shielding the magnitude of the eddy currents in the cryostat is reduced. An approximately 4.0% preemphasis overshoot was required, and yet variation in axial coil positions remains advantageous for producing the best coil performance. The unshielded gradient coil (Fig. 4 and Table 3) is around 1.46 times more efficient than the shielded gradient coil (Fig. 9 and Table 4) under the same transport current conditions. Obviously, displacing the active shield further away from the primary coil would improve the gradient efficiency. However, the unshielded coil requires much more voltage overdrive (Fig. 4) than the actively shielded gradient and hence imposes a greater burden on the amplifier system. The final result of these gradient-coil optimizations is not a highly stable gradient waveform, but rather a gradient waveform that is stable enough to be corrected using typical magnitudes of amplifier preemphasis. The final system specification for gradient waveform fidelity on clinical scanners is typically on the order of 0.02% (after eddy-current calibrations are completed).

Figure 10 illustrates the effects of preemphasis and perturbed current distribution on the spatial and temporal characteristics of the induced eddy currents in cases of shielded and unshielded *z*-gradients. Four cases are considered: 1) eddy-current nonoptimized single-layer, 2) eddy-current optimized single-layer, 3) eddy-current nonoptimized actively shielded *z*-gradient coil, and 4) eddy-current optimized actively shielded *z*-gradient coil. As expected, the flow direction of induced eddy currents at 100 μs is opposite to the nearest gradient currents, while the eddy-current temporal variation resembles the switching sequence employed (trapezoidal: 1 kHz frequency, 100 μs rise time) in driving the gradient coils. At 0.5 ms, the eddy currents are reversed in direction to counteract the new current direction in the gradient coils. In all cases the largest eddy currents are induced in the second cryostat wall, as this is the first EM shield with reasonably high material conductivity. The EM energy diffuses slowly through this second layer and, as expected, the eddy current excitation in the third wall is considerably delayed in time. The current overshoot in the optimized unshielded (single-layer) *z*-gradient is evident. In addition, one can observe different decay terms within the cryostat vessel due to diverse material properties and unique wall geometries within the cryostat vessel.

CONCLUSIONS

Longitudinal gradient coils can be implemented to produce very uniform gradient fields over time by taking into account the transient eddy currents induced in the cryostat vessel. The compensation can be achieved through coupled optimization of spatial distribution and preemphasis of the gradient-coil current that accounts for the presence of the eddy-current field, and should be preferably applied during the design process of the gradient coil. Through a priori spatial correction of eddy-current fields, the preemphasis can be tailored to achieve improved target field uniformities over time under different rise-time conditions. In future work, we intend to study the implication of different imaging sequences, rise times, and gradient coil/cryostat vessel geometries on the target gradient uniformity using this new method. Furthermore, we plan to extend the method to three dimensions and apply parallelism to the algorithm in order to make eddy-current optimization of transverse gradient coils possible.

The proposed method provides distinct advantages for systems engineering of gradient coil/magnet pairs because the cryostat and gradient set can be designed together in terms of eddy-current induction and field profiles. This also allows the rapid design and prototyping of cryostats of various shapes and properties.

REFERENCES

1. Badea EA, Craiu O. Eddy current effects in MRI super-conducting magnets. IEEE Trans Magn 1997;33:1330–1333.
2. Ries G. Eddy current transients and forces in cryostat walls of superconducting solenoids. IEEE Trans Magn 1988;24:516–519.
3. Shvartsman S, Morich M, Demeester G, Zhai Z. Ultrashort shielded gradient coil design with 3D geometry. Concepts Magn Reson Part B 2005;26B:1–15.
4. Mansfield P, Chapman B. Active magnetic screening of static and time-dependent magnetic field generation in NMR imaging. J Phys E Sci Instrum 1988;19:540:545.
5. Crozier S, Doddrell DM. A design methodology for short, whole-body, shielded gradient coils for MRI. Magn Reson Imaging 1995;13:615–620.
6. Jehenson P, Westphal M, Schuff N. Analytical method for the compensation of eddy-current effects induced by pulsed magnetic field gradients in NMR systems. J Magn Reson 1990;90:264–278.
7. Bowtell R, Mansfield P. Gradient coil design using active magnetic screening. Magn Reson Med 1991;17:15–21.
8. Brown RW, Shvartsman S. Supershielding: confinement of magnetic fields. Physics Rev Lett 1999;83:1946–1949.
9. Gach HM, Lowe IJ, Madio DP, Caprihan A, Altobelli SA, Kuethe DO, Fukushima E. A programmable preemphasis system. J Magn Reson Med 1998;40:427–431.
10. Crozier S, Eccles CD, Beckey FA, Fields J, Doddrell DM. Correction of eddy-current-induced B_0 shifts by receiver reference-phase modulation. J Magn Reson 1992;97:661–665.
11. Liu F, Crozier S. An FDTD model for calculation of gradient-induced eddy currents in MRI system. IEEE Trans Appl Superconduct 2004;14:1983–1989.
12. Trakic A, Wang H, Liu F, Sanchez Lopez H, Crozier S. Analysis of transient eddy currents in MRI using a cylindrical FDTD method. IEEE Trans Appl Superconduct 2006;16:1924–1936.
13. Turner R, Bowley RM. Passive screening of switched magnetic field gradients. J Phys E Sci Instrum 1986;19:876–879.
14. Taflove A. Computational electromagnetics—the finite-difference time-domain method. London: Artech; 1995.
15. Turner R. Gradient coil design: a review of methods. Magn Reson Imaging 1993;11:903–920.
16. Abramowitz M, Stegun IA. Handbook of mathematical functions. London: Dover; 1965.
17. Ahhn CB, Cho ZH. Analysis of eddy currents in nuclear magnetic resonance imaging. Magn Reson Med 1991;17:149–163.
18. Wang H, Trakic A, Liu F, Bialkowski ME, Crozier S. A high performance FDTD scheme for MRI. In: Proceedings of the 14th Annual Meeting of ISMRM, Seattle, WA, USA, 2006 (Abstract 1385).